A 50-kW Three-Channel Wireless Power Transfer System With Low Stray Magnetic Field

Abubakar Uba Ibrahim, *Student Member, IEEE*, Wenxing Zhong, *Member, IEEE*, and Mark Dehong Xu, *Fellow, IEEE*

***Abstract*—Adopting high-power wireless charging systems, particularly for heavy-duty electric vehicles (EVs) and fast charging of regular EVs, becomes extremely imperative. The stringent requirements of safety guidelines, high efficiency, and high-power density would continue to impede the rapid penetrations of wireless power transfer (WPT) systems for EVs at high power. This article investigates the potentials of multichannel WPT systems to achieve high-power transmission under such requirements. A multichannel WPT system consists of multiple power-transfer paths such that adjusting the number of channels affords the system become adaptive to multiple power levels that could eventually present an opportunity for developing high power, which would be seriously challenging with the conventional single-channel systems. Moreover, different channels can cooperate to achieve superior performance, such as a low stray magnetic field. A three-channel WPT system is designed in this article, and its capability of significantly reducing the stray magnetic field is investigated. By properly determining the power-sharing proportion of the channels, the magnetic field reduction of 80% and 63% can be achieved compared with the rectangular-pad and double D (DD) pad systems (under similar total pads area), respectively. A three-channel 50-kW prototype is produced with a dc–dc efficiency of 95.2% across the 160 mm air gap. The measured results of the magnetic field agree well with the simulation ones.**

***Index Terms*—Wireless power transfer, inductive power transfer, multi-channel WPT.**

I. Introduction

ALTHOUGH its first proposition by Nicola Tesla was more than a century ago [1], [2], magnetic resonant wireless power transfer (WPT) has been gaining ground, and the technology is rapidly maturing. Recently, it is widely used for charging industrial equipment, cellphones, electric vehicles (EVs), etc. [3]–[5]. A clear demand for developing fast wireless charging facility as well as charging heavy-duty EVs incentivizes a rapid increase of the power level of the WPT. Besides the high-power (above 50 kW) systems developed for dynamic charging [6]–[8], considerable efforts have been made in developing high-power stationary WPT with 50 kW or above [9]–[11].

Manuscript received November 9, 2020; revised February 4, 2021; accepted March 3, 2021. Date of publication March 8, 2021; date of current version June 1, 2021. This work was supported by the National Natural Science Foundation of China under Grant 51807174. Recommended for publication by Associate Editor J. M. Rivas Davila. *(Corresponding authors: Wenxing Zhong and Mark Dehong Xu.)*

The authors are with the Institute of Power Electronics, Zhejiang University, Hangzhou 310027, China (e-mail: habuuba@zju.edu.cn; wxzhong@zju.edu.cn; xdh@zju.edu.cn).

Digital Object Identifier 10.1109/TPEL.2021.3064373

One critical issue of the high-power WPT is its intense stray magnetic field emissions, which is a big challenge to meet the safety restrictions. To promote the compliance of safety guidelines by the International Commission of Nonionizing Radiation Protection, the Society of Automotive Engineers (SAE) recommends the maximum magnetic field exposure of 27 μT rms and 15 μT rms for the general public and possible people with body-implanted medical device, respectively [12], [13]. Table I summarizes a few reported results of the stray magnetic field generated by various WPT systems. The measuring point is outside the area covered by the vehicle, which is about 0.8 m from the center point of the coupled pads (i.e., in the middle of the air gap), which falls under region 2a according to the provision of SAE J2954 [13]. If there is a misalignment, this center point will be unchanged with respect to the vehicle. The 50 kW WPT system, as presented in [9], has a stray magnetic flux density of approximately 24 μT rms. While in [14], the stray B-field of a 3.3 kW system slightly exceeds the safety limit, which might be mainly due to the large misalignment. Therefore, it is reasonable to deduce that a similar system to the one in [9] might violate the safety limit of 27 μT rms if a large misalignment occurs. Moreover, magnetic flux density grows proportionately to the square root of the power level [15], which implies that it is more challenging to design the high-power WPT systems under this safety constraint.

Shielding methods based on generating counter magnetic fields have been widely adopted to cancel out the stray magnetic field and weakens the flux density at the interested positions. There is generally passive shielding [16]–[21] and active shielding [22], [23]. Passive shielding has an upper limit in terms of shielding effectiveness [24], and active shielding usually requires extra installation space and increases the complexity of the whole system [23].

Polyphase WPT systems could essentially be effective in reducing stray magnetic fields comparing with single-phase systems. For example, the 50-kW system using double D (DD) pads has a large reduction in the stray magnetic field compared with its counterpart using rectangular pads [9], as given in Table I. However, it is appropriate to note that DD pads WPT systems can be regarded as a two-phase system whose windings of the two phases are connected in series with the opposite winding directions. This structure was later developed into a bipolar pad (BPP) whose two windings are decoupled by adding an overlap [25]. Apart from DD and BPP, which are virtually two phases, numerous studies have been carried

TABLE I
STRAY MAGNETIC FLUX DENSITY OF WPT SYSTEMS

Ref.	Power [kW]	Winding Structure	Pad Size [m^2][a]	Air Gap [mm]	Operating Frequency [kHz]	Conductive Shielding Layer	Misalignment [mm]	B-field [μT RMS]
[9]	50	Rectangular	0.24	160	85	Smaller than coi [b]	0	24
	50	DD	0.24	160	85	Smaller than coil[b]	0	13
[10]	50	Bipolar (three-phase)	0.26	180	88.5	None	0	34.7
[14]	3.3	Pri.: Tripolar pad Sec.: Circular pad	0.35 0.2	150	20	Same size as the pads	(150, 150)	28.7

[a]Including coil and ferrite.
[b]Shielding in these systems is designed to reduce eddy current loss in the resonant capacitor rather than to eliminate the stray magnetic field.

out on three-phase WPT systems [26]–[32]. However, almost all of the polyphase WPT systems share a common problem, which is known as interphase cross coupling. Cross couplings in the context of this article include all other couplings except the main primary–secondary coupling of each channel. The major effect of the cross couplings is causing unbalance power sharing and power circulation among phases [33]–[36], etc. Thus, it causes the degradation of power transfer capability and efficiency of polyphase WPT. The cross couplings of the coils in the same side (i.e., either primary side or secondary side) can be largely reduced by using the partially overlapping structure as a BPP [14] or by mere adjustment of magnetic couplings among the primary (or secondary) coil [35]. It is also possible to eliminate the adverse effects of the same-side cross couplings by a proper design of compensations [31], [37]. However, for those multiphase systems with identical pads in both the primary and secondary sides, there are still interphase couplings between the coils from different sides. The diagonal placement of the magnetic pads containing four-solenoid windings, as proposed in [36], drastically reduces the unwanted cross couplings, but this approach cannot be directly applied to circular pads.

This article investigates the potential of a multichannel WPT system to achieve superior performance. By adjusting the number of channels, the power level of a multichannel system can be adaptive to many different applications and a lot of effort on designing and testing new systems can be saved. Another major merit of multichannel WPT is that the stray magnetic fields generated by different channels can be controlled to cancel out each other, thereby significantly attenuating the extended stray magnetic flux density. As an example, a three-channel WPT system is designed and the cross couplings are minimized. To leverage the ability of flux cancelations due to currents phase angle difference in multichannel WPT systems, a study is undertaken to demonstrate the extent of stray magnetic field reduction (which is critical for high-power WPT). A prototype of 50 kW is built, and the experimental results are consistent with the simulation results.

The rest of the article is arranged as follows. Section II presents the general concept of multichannel WPT systems as well as the theory of magnetic field cancelations. Section III discusses the effects of cross couplings. Section IV gives the design of a practical three-channel WPT system and investigates the potential of multichannel WPT systems in attenuating stray magnetic field through case studies. The experimental verification is presented in Section V. Finally, Section VI concludes the article.

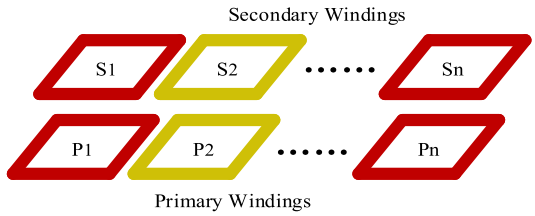

Fig. 1. Multichannel WPT system.

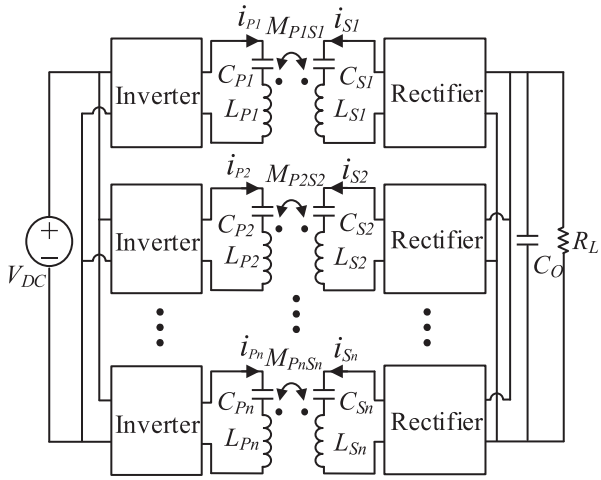

Fig. 2. Circuit topology of a multichannel WPT system (cross mutual inductances not shown).

II. MULTICHANNEL WPT

A. General Concept

Fig. 1 shows the general schematic of a multiple-channel WPT system with n channels and Fig. 2 shows the circuit topology of the system. Each channel is basically the traditional WPT system consisting of one primary-side inverter, a pair of coupled LC resonators, and a secondary-side rectifier. The circuit model of n-channel series–series compensated WPT system is given

by (1) [48], where subscripts *P* and *S* denote the primary side and secondary side, respectively; R_i ($i = P1, S1, \ldots, P_n, S_n$) is the parasitic resistance [the sum of the resistance of winding-*i*, the equivalent series resistance (ESR) of capacitor-*i*]; X_i is the reactance (ωL_i-$1/(\omega C_i)$), L_i is the inductance, and C_i is the capacitance; I_i is the current in resonator *i*; M_{ij} is the mutual inductance between resonators *i* and *j*; U_{Pq} and R_{LSq} ($q = 1, 2, \ldots, n$) are the voltage source and the load resistance of channel-*q*, respectively; and ω is the operating angular frequency.

As indicated in (1), all the cross couplings will participate in the operation of the system, forming power flowing paths for either active power or reactive power. However, the most efficient power path for transferring active power from the source to the load is formed by the main coupling of each channel (M_{PxSx}) because these main couplings are expected to have a higher coupling coefficient *k* relative to other cross couplings. Therefore, all the power paths created by cross couplings might degrade the performance of the system in terms of efficiency (due to circulating power paths) and power transfer capability (due to reactive power). In addition, these cross couplings could also complicate the control of the system.

B. Analysis of Stray Magnetic Field

In a multichannel WPT system, the phase angles of the winding currents, as well as the ratio of magnetomotive force (MMF), i.e., the product of the number of turns *N* and the current of a winding *I*, will affect the stray B-field of the system. This is first investigated through theoretical calculation without considering ferrite layers and shielding layers for simplicity. The method to calculate the B-field generated by one or multiple windings is reported in [38] and [39] and will be repeated as follows.

The magnetic flux density of a rectangular loop at a point *P*(*x, y, z*) is determined by the total contribution of each segment of the loop [38]–[40]. Fig. 3 depicts the positioning of multiple rectangular coils. The origin of the coordinate system is located at the center of Coil-1. For Coil-*h* ($h = 1, 2, 3, \ldots, n$), its current is denoted as $i_h(t)$; the number of turns is denoted as N_h; the outer dimension of the coil is denoted as $2a_h$ by $2b_h$; the distance between its center and the origin is denoted as d_h; the distance between two neighboring turns is denoted as d_{Th}; and the distance between each corner of the *s*th turn ($s = 1, 2, 3, \ldots, N_h$) of Coil-*h* to the observation point *P* is described as r_{hs1}, r_{hs2}, r_{hs3}, and r_{hs4}, where the subscripts *h* and *s* represent Coil-*h* and the *s*th turn of Coil-*h*, respectively. The total magnetic field due to the alternating currents flowing through the coils can be described by the vector [38]

$$\vec{B}_T\ (t) = B_x\,\vec{i} + B_y\vec{j} + B_z\vec{k} \tag{2}$$

where

$$B_x = \sum_{h=1}^{n} \frac{\mu_0 i_h\,(t)}{4\pi} \sum_{s=1}^{N_h} \left(\begin{array}{l} \frac{z}{r_{hs1}(r_{hs1}+d_{hs1})} - \frac{z}{r_{hs2}(r_{hs2}+d_{hs2})} \\ + \frac{z}{r_{hs3}(r_{hs3}+d_{hs3})} - \frac{z}{r_{hs4}(r_{hs4}+d_{hs4})} \end{array} \right)$$

$$B_y = \sum_{h=1}^{n} \frac{\mu_0 i_h\,(t)}{4\pi} \sum_{s=1}^{N_h} \left(\begin{array}{l} \frac{z}{r_{hs1}(r_{hs1}+C_{hs1})} - \frac{z}{r_{hs2}(r_{hs2}-C_{hs2})} \\ + \frac{z}{r_{hs3}(r_{hs3}+C_{hs3})} - \frac{z}{r_{hs4}(r_{hs4}-C_{hs4})} \end{array} \right)$$

$$B_y = \sum_{h=1}^{n} \frac{\mu_0 i_h\,(t)}{4\pi} \sum_{s=1}^{N_h} \left(\begin{array}{l} -\frac{d_{hs1}}{r_{hs1}(r_{hs1}+C_{hs1})} - \frac{C_{hs1}}{r_{hs1}(r_{hs1}+d_{hs1})} \\ + \frac{d_{hs2}}{r_{hs2}(r_{hs2}-C_{hs2})} - \frac{C_{hs2}}{r_{hs2}(r_{hs2}+d_{hs2})} \\ - \frac{d_{hs3}}{r_{hs3}(r_{hs3}+C_{hs3})} - \frac{C_{hs3}}{r_{hs3}(r_{hs3}+d_{hs3})} \\ + \frac{d_{hs4}}{r_{hs4}(r_{hs4}-C_{hs4})} - \frac{C_{hs4}}{r_{hs4}(r_{hs4}+d_{hs4})} \end{array} \right)$$

$$r_{hs1} = \sqrt{C_{hs1}^2 + d_{hs1}^2 + z^2}$$

$$r_{hs2} = \sqrt{C_{hs2}^2 + d_{hs2}^2 + z^2}$$

$$r_{hs3} = \sqrt{C_{hs3}^2 + d_{hs3}^2 + z^2}$$

$$r_{hs3} = \sqrt{C_{hs4}^2 + d_{hs4}^2 + z^2}$$

$$d_{hs1} = d_{hs2} = y - d_h + b_h - (s-1)\,d_{Th}$$

$$d_{hs3} = d_{hs4} = y - d_h - b_h + (s-1)\,d_{Th}$$

$$C_{hs1} = -C_{hs4} = x + a_h - (s-1)\,d_{Th}$$

$$C_{hs2} = -C_{hs3} = -x + a_h - (s-1)\,d_{Th}.$$

To investigate the effects of the phase difference of the winding currents and the ratio of *NI* (i.e., the product of the number of turns and the current of a winding) on the stray magnetic field, we take a three-channel WPT system as an example. To maintain generality, we use single-turn coils to represent ordinary flat windings. Totally, there are three channels and six identical coils, i.e., Channel 1 with Coil-*P*1 (primary) and *S*1 (secondary), Channel 2 with Coil-*P*2 and *S*2, and Channel 3 with Coil-*P*3 and *S*3, as shown in Fig. 4. The distance between the centers of the primary and secondary windings is 160 mm. The coil dimension is 0.3 m by 0.3 m, and the distance between the centers of each adjacent coil is 0.5 m. The origin of the coordinate system is located at the center of Coil-*P*1. The observation plane ($x = -0.8$ m) is 0.8 m away from the center of the coils (along the $-X$-direction). Three primary windings share 10 A current, and three secondary windings also share 10 A current. First, equal current sharing, i.e., each coil carrying 3.33 A, is investigated with different current phases. The phase angles of the currents are denoted as $\theta_{P1}, \theta_{P2}, \theta_{P3}, \theta_{S1}, \theta_{S2}$, and θ_{S3} for Coil-*P*1, *P*2, *P*3, *S*1, *S*2, and *S*3, respectively. It should be noted that each of the

$$\begin{bmatrix} R_{P1}+jX_{P1} & j\omega M_{P1S1} & j\omega M_{P1P2} & \cdots & j\omega M_{P1Pn} \\ j\omega M_{P1S1} & R_{S1}+R_{LS1}+jX_{S1} & j\omega M_{S1P2} & \cdots & j\omega M_{S1Pn} \\ j\omega M_{P1P2} & j\omega M_{S1P2} & R_{P2}+jX_{P2} & \cdots & j\omega M_{P2Pn} \\ \vdots & \vdots & \vdots & \ddots & \vdots \\ j\omega M_{P1Sn} & j\omega M_{S1Sn} & j\omega M_{P2Sn} & \cdots & R_{Sn}+R_{LSn}+jX_{Sn} \end{bmatrix} \cdot \begin{bmatrix} \overrightarrow{I_{P1}} \\ \overrightarrow{I_{S1}} \\ \overrightarrow{I_{P2}} \\ \vdots \\ \overrightarrow{I_{Sn}} \end{bmatrix} = \begin{bmatrix} \overrightarrow{U_{P1}} \\ 0 \\ \overrightarrow{U_{P2}} \\ \vdots \\ 0 \end{bmatrix} \tag{1}$$

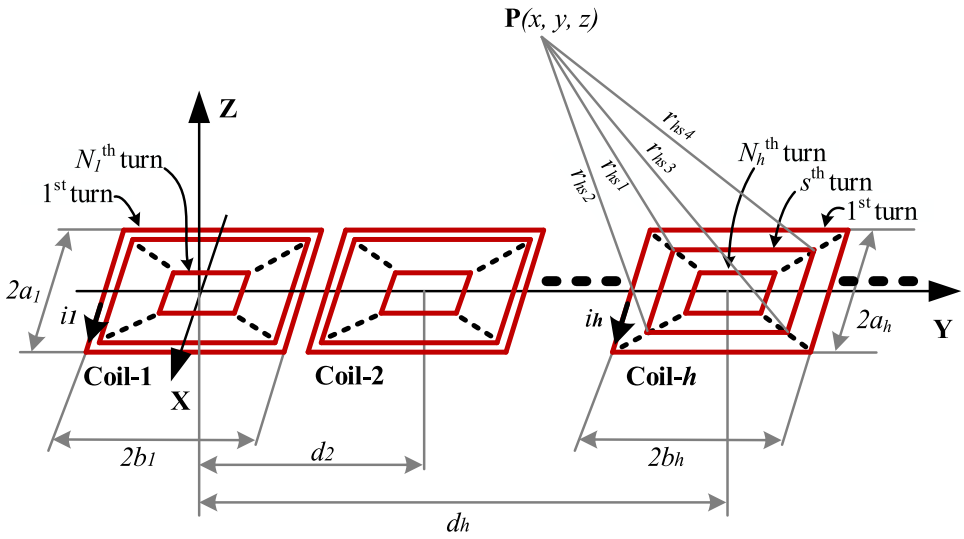

Fig. 3. Multiple rectangular windings placed in a straight line.

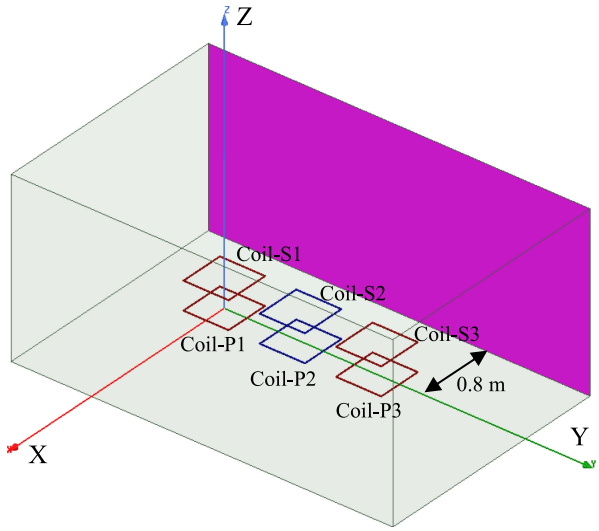

Fig. 4. Winding structure of an example three-channel WPT system and the position of the observation plane of the stray B-field.

secondary currents should normally lag the respective primary current of the same channel by 90° in order to efficiently transfer active power, i.e., $\theta_{S1} = \theta_{P1} - 90°$, $\theta_{S2} = \theta_{P2} - 90°$, and $\theta_{S3} = \theta_{P3} - 90°$. Based on (2), the maximum B-field of each point on the observation plane can be calculated. Fig. 5 shows the B-field plots on the observation plane of three cases in which we assume $\theta_{P2} = 0°$.

1) The currents of the same side are in-phase, i.e., $\theta_{P1} = \theta_{P2} = \theta_{P3} = 0°$ and $\theta_{S1} = \theta_{S2} = \theta_{S1} = -90°$.
2) Each of the currents is 120° out of phase to the other two in the same side, i.e., $\theta_{P1} = -120°$ (or 120°), $\theta_{P2} = 0°$, and $\theta_{P3} = 120°$ (or $-120°$), and $\theta_{S1} = -210°$ (or 30°), $\theta_{P2} = -90°$, and $\theta_{P3} = 30°$ (or $-210°$).
3) The aside coil currents are 180° out of phase to the middle coil currents, i.e., $\theta_{P1} = 180°$, $\theta_{P2} = 0°$, and $\theta_{P3} = 180°$, and $\theta_{S1} = 90°$, $\theta_{P2} = -90°$, and $\theta_{P3} = 90°$.

The calculated results are confirmed with finite-element simulation results. From Fig. 5, it can be seen that both the case with 180° current phase difference and the case with 120° current phase difference provide significant B-field reduction compared with that of the case with in-phase currents, and the case with 180° current phase difference is the best among the three.

It is also motivational to ascertain the influence of the ratio of the product of the number of turns and current (*NI*) since the contribution to the magnetic field by each coil is dictated by *NI*. It is, therefore, very relevant to determine the optimal *NI* ratio among the channels in such a manner that the magnetic field cancelations could be optimal. This case study is also based on the above three-channel system with single-turn coils. Therefore, the *NI* ratio becomes the current ratio. The total current in the described three-channel system is 10 A on both the primary and secondary sides. The current amplitudes of two aside channels are assumed identical, i.e., $I_{P1} = I_{P3}$ and $I_{S1} = I_{S3}$. The current ratio is then defined as the ratio between the current of the aside channels and the current of the middle channel, e.g., I_{P1} (or I_{P3})/I_{P2}. We also assume I_{S1}/(or I_{S3})/$I_{S2} = I_{P1}/I_{P2}$, which is normally valid in a parallel input and parallel output multichannel system. Fig. 6 shows the calculated and simulation results of the maximum B-field on the said observation plane under different current ratios and different current phase differences of 120° ($\theta_{P1} = -120°$, $\theta_{P2} = 0°$, and $\theta_{P3} = 120°$, and $\theta_{S1} = -210°$, $\theta_{P2} = -90°$, and $\theta_{P3} = 30°$) and 180° ($\theta_{P1} = 180°$, $\theta_{P2} = 0°$, and $\theta_{P3} = 180°$, and $\theta_{S1} = 90°$, $\theta_{P2} = -90°$, and $\theta_{P3} = 90°$), respectively. The optimal point is found when the current ratio is 0.7 (i.e., Channel-2 outputs about 40% of the total power) and the current phase difference is 180°. For the case with a 120° current phase difference, changing the current ratio barely affects the minimal stray B-field.

Magnetic ferrite layers are necessary for most of the real-life applications of WPT. It is, therefore, imperative to evaluate whether the ferrite cores can lead to any significant alteration on the B-field results. Simulations are performed on the three-channel system with plate ferrites, as shown in Fig. 7. The

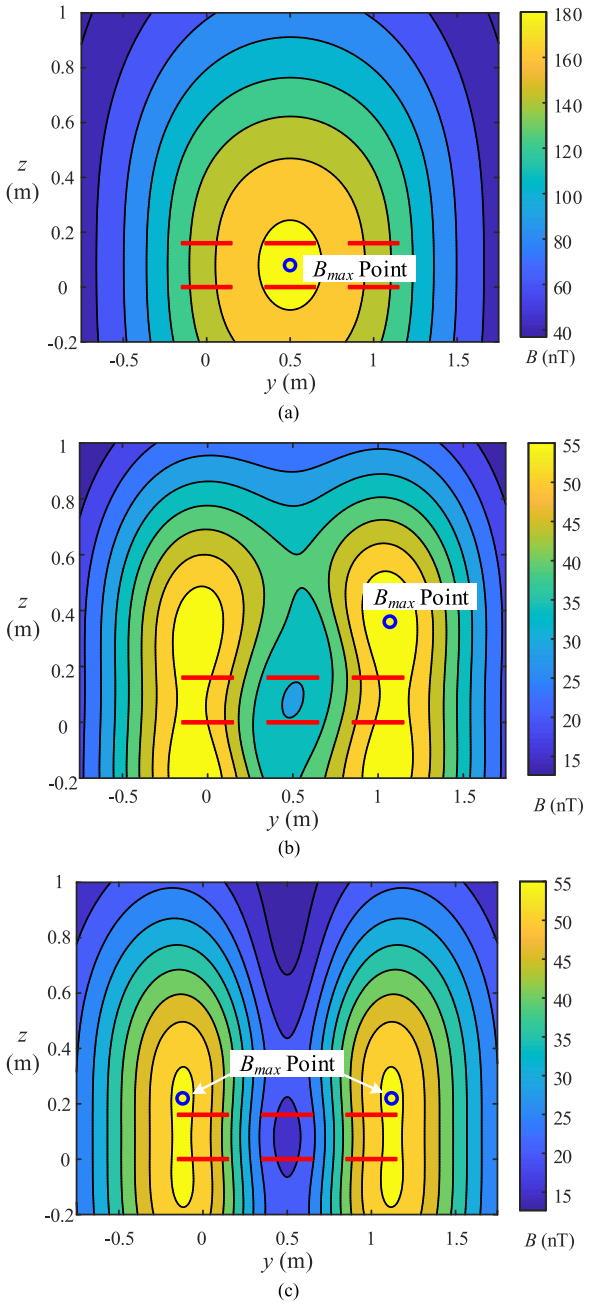

Fig. 5. Calculated maximum B-field on the observation plane with identical current amplitude and different current phase differences among channels. [Red bars represent the projections of the windings on the plane.] (a) In-phase—calculated $B_{\max}$ 184 nT (simulation value 188 nT). (b) −120°, 0°, 120°—calculated $B_{\max}$ 58.9 nT (simulation value 58.5 nT). (c) 180°, 0°, 180°—calculated $B_{\max}$ is 55.8 nT (simulation value 56.2 nT).

results are given in Fig. 8 and compared with the results in Fig. 6. As shown in Fig. 8, the ferrites only slightly enhance the stray magnetic field compared with the simulation results of the system without ferrite.

III. Effects of Cross Couplings

For a multichannel WPT system, the critical challenge is the cross couplings among every two different channels. To clarify the effects of these cross couplings, theoretical analysis and

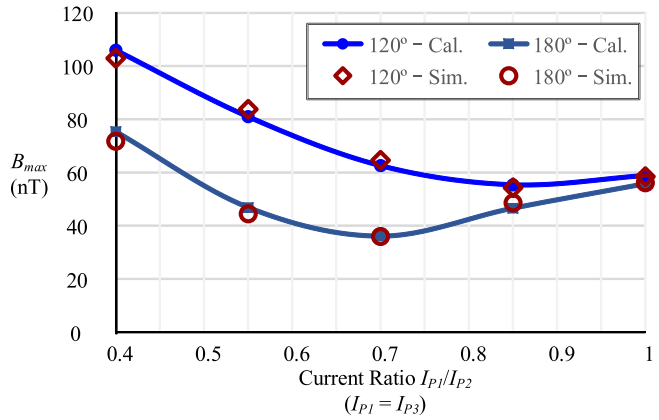

Fig. 6. Variation of stray magnetic flux density on the observation plane with the current ratio.

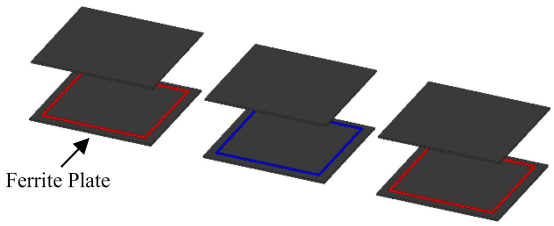

Fig. 7. Three-channel WPT system with ferrite layers.

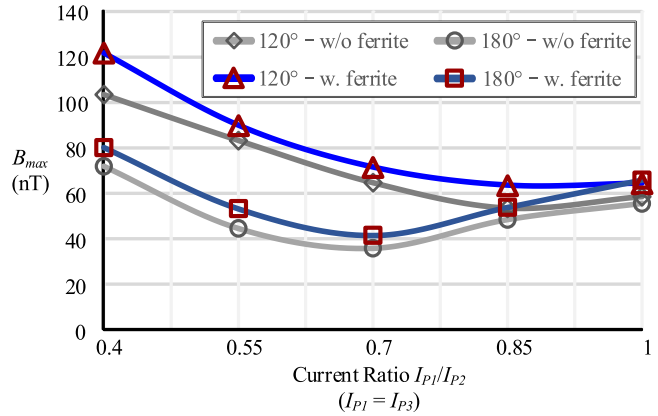

Fig. 8. Effect of ferrites core on the stray magnetic flux density on the observation plane with current ratio. [Ferrite plate dimension: 350 mm × 350 mm × 5 mm; and the gap between ferrite and winding: 1 mm.].

a case study are provided as follows based on a two-channel WPT system (i.e., *P*1–*S*1 and *P*2–S2). The parameters of the two channels are identical, i.e., $M_{P1S1} = M_{P2S2}$, $R_{P1} = R_{P2}$, $R_{S1} = R_{S2}$, and $R_{LS1} = R_{LS2}$. The operating frequency equals the resonant frequency of the resonators, i.e., $X_{P1} = X_{P2} = X_{S1} = X_{S2} = 0$. The circuit equations of the system are

$$R_{P1}\vec{I}_{P1} + j\omega M_{P1P2}\vec{I}_{P2} + j\omega M_{P1S1}\vec{I}_{S1} + j\omega M_{P1S2}\vec{I}_{S2} = \vec{U}_{P1} \quad (3)$$

$$j\omega M_{P1P2}\vec{I}_{P1} + R_{P2}\vec{I}_{P2} + j\omega M_{P2S1}\vec{I}_{S1} + j\omega M_{P2S2}\vec{I}_{S2} = \vec{U}_{P2} \quad (4)$$

$$j\omega M_{P1S1}\vec{I}_{P1}+j\omega M_{P2S1}\vec{I}_{P2}+(R_{S1}+R_{LS1})\vec{I}_{S1}+j\omega M_{S1S2}\vec{I}_{S2}=0 \quad (5)$$

$$j\omega M_{P1S2}\vec{I}_{P1}+j\omega M_{P2S2}\vec{I}_{P2}+j\omega M_{S1S2}\vec{I}_{S1}+(R_{S2}+R_{LS2})\vec{I}_{S2}=0. \quad (6)$$

If the secondary currents $\vec{I}_{S1}$ and $\vec{I}_{S2}$ are given (e.g., the secondary currents are with the same required amplitude and 180° out of phase to minimize the B-field), the primary currents $\vec{I}_{P1}$ and $\vec{I}_{P2}$ can be determined by solving (5) and (6) as [49]

$$\vec{I}_{P1}=\frac{[j\omega M_{P2S1}M_{S1S2}-M_{P2S2}(R_{S1}+R_{LS1})]\vec{I}_{S1}+[M_{P2S1}(R_{S2}+R_{LS2})-j\omega M_{S1S2}M_{P2S2}]\vec{I}_{S2}}{j\omega(M_{P1S1}M_{P2S2}-M_{P1S2}M_{P2S1})} \quad (7)$$

$$\vec{I}_{P2}=\frac{[j\omega M_{P1S1}M_{S1S2}-M_{P1S2}(R_{S1}+R_{LS1})]\vec{I}_{S1}+[M_{P1S1}(R_{S2}+R_{LS2})-j\omega M_{S1S2}M_{P1S2}]\vec{I}_{S2}}{-j\omega(M_{P1S1}M_{P2S2}-M_{P1S2}M_{P2S1})}. \quad (8)$$

A. Primary-Side Cross Coupling

It should be noted that the primary-side cross mutual inductance M_{P1P2} is not required in (7) and (8). In other words, M_{P1P2} does not affect the calculation of $\vec{I}_{P1}$ and $\vec{I}_{P2}$ when $\vec{I}_{S1}$ and $\vec{I}_{S2}$ are given. Under this condition, M_{P1P2} does not affect the system efficiency. This principle is the same as that in a single-channel system, i.e., the compensating condition of the primary resonator will not affect the power transfer efficiency of the coupled resonators.

On the other hand, it is clear from (3) and (4) that M_{P1P2} will affect the required input voltages U_{P1} and U_{P2} to generate the desired secondary currents.

B. Secondary-Side Cross Coupling

First, the diagonal cross couplings, i.e., M_{P2S1} and M_{P1S2}, are assumed to be zero. We examine the difference in the primary currents to output the same amount of secondary currents (i.e., given I_{S1} and I_{S2}, and $I_{S1}=I_{S2}$) when the secondary-side cross coupling M_{S1S2} is zero or nonzero.

With zero M_{S1S2}, the required primary currents to output I_{S1} and I_{S2} are given as follows, according to (5) and (6):

$$I_{P1}=\frac{(R_{S1}+R_{LS1})I_{S1}}{\omega M_{P1S1}} \quad (9)$$

$$I_{P2}=\frac{(R_{S2}+R_{LS2})I_{S2}}{\omega M_{P2S2}}. \quad (10)$$

The power loss in the primary resonators is

$$I_{P1}^2R_{P1}+I_{P2}^2R_{P2}=2\frac{(R_{S1}+R_{LS1})^2I_{S1}^2}{\omega^2M_{P1S1}^2}R_{P1}. \quad (11)$$

With nonzero M_{S1S2}, we take $\vec{I}_{S1}$ as the reference (with a phase angle of zero). We assume that the other secondary current has the same amplitude and an arbitrary phase angle. So, its phasor representation is

$$\vec{I}_{S2}=I_{S1}\angle\theta_{S2}. \quad (12)$$

According to (5) and (6), the primary currents are given by

$$\vec{I'}_{P1}=\frac{-(R_{S1}+R_{LS1})\vec{I}_{S1}-j\omega M_{S1S2}\vec{I}_{S2}}{j\omega M_{P1S1}} \quad (13)$$

$$\vec{I'}_{P2}=\frac{-j\omega M_{S1S2}\vec{I}_{S1}-(R_{S2}+R_{LS2})\vec{I}_{S2}}{j\omega M_{P2S2}}. \quad (14)$$

It can be seen from (13) and (14) that the phase difference between two secondary currents largely affects the amplitudes of the primary currents. For example, if $\theta_{S2}=0$ or 180°, both I'_{P1} and I'_{P2} increase; if $\theta_{S2}=90°$ and $M_{S1S2}<0$ (as for two planar windings put side-by-side), I'_{P1} increases and I'_{P2} decreases.

With (12), the power loss in the primary resonators can be calculated as

$$I'^2_{P1}R_{P1}+I'^2_{P2}R_{P2}=2\frac{\left[(R_{S1}+R_{LS1})^2+\omega^2M_{S1S2}^2\right]I_{S1}^2}{\omega^2M_{P1S1}^2}R_{P1}. \quad (15)$$

By comparing (11) and (15), it can be seen that the primary loss increases as $|M_{S1S2}|$ increases and the efficiency is independent of the phase difference of the secondary currents.

C. Intersides Cross Coupling

Generally, intersides cross couplings, such as M_{P1S2}, provide additional power paths between the primary windings and secondary windings. The power paths might deliver real power or reactive power or both, depending on the phase difference between two currents in the coupled windings. If only the real power is delivered from the primary winding to the secondary winding, it means the same primary current can generate higher output power compared with the counterpart with zero intersides cross couplings. Therefore, the efficiency of the system can be improved. By contrast, if the real power is delivered from the secondary winding to the primary winding, a circulating power loop is formed in the system, which leads to lower power transfer efficiency.

A case study is provided based on an imaginary two-channel WPT system, whose parameters are listed in Table II. For each independent channel, the output power is 3.3 kW at the given load resistance; the primary voltage applied to the resonator is $V_{P0}=185.9$ V; the primary resonator current $I_{P0}=17.75$ A; and the power transfer efficiency is 98%.

The calculation results of the efficiency, the input voltages (V_{px}, $x=1$ or 2), which are normalized to V_{P0}, the primary currents (I_{px}, $x=1$ or 2), which are normalized to I_{P0}, and the phase difference between two primary currents, under variations of the phase difference of two secondary currents, are shown

TABLE II
PARAMETERS OF AN IMAGINARY TWO-CHANNEL WPT SYSTEM

L_{P1}, L_{P2}, L_{S1}, L_{S2}	R_{P1}, R_{P2}, R_{S1}, R_{S2}	f, R_L	I_{S1}, I_{S2}
100 μH	0.1068 Ω @ 85 kHz ($Q = 500$)	85 kHz, 10.68 Ω	17.58 A
k_{P1S1}, k_{P2S2}	k_{P1P2}	k_{S1S2}	k_{P1S2}, k_{P2S1}
0.2	variable	variable	variable

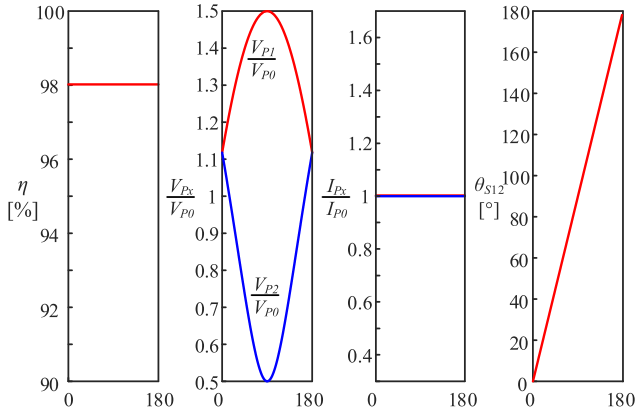

Fig. 9. Efficiency, input voltage, primary currents, and phase difference between two primary currents as functions of the phase difference of two secondary currents for the system with $k_{P1P2} = -0.1$ (other cross couplings are zero).

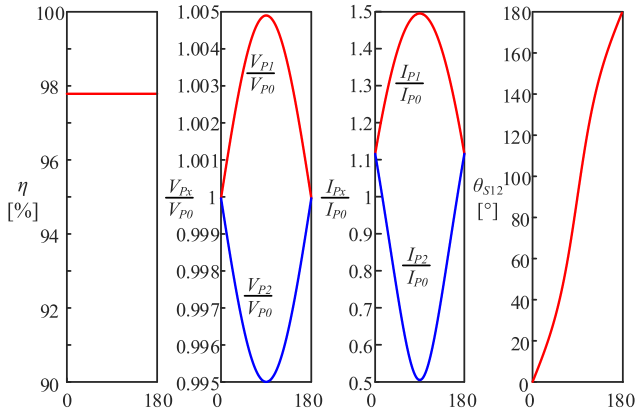

Fig. 10. Efficiency, input voltage, primary currents, and phase difference between two primary currents as functions of the phase difference of two secondary currents for the system with $k_{S1S2} = -0.1$ (other cross couplings are zero).

in Figs. 9–11 for the system with $k_{P1P2} = -0.1$ (other cross couplings are zero), $k_{S1S2} = -0.1$(other cross couplings are zero), and $k_{P1S1} = k_{P2S1} = 0.1$ (other cross couplings are zero), respectively.

As revealed in the above analysis and verified in Fig. 9, the primary cross coupling does not affect either the system efficiency or the primary-side currents. However, the input voltages of the two channels become unbalanced if the phase difference of two secondary currents is not 0° or 180°. Nevertheless, when the phase difference of two secondary currents is 180° as desired to realize the low stray B-field, the input voltages are 10% higher than that of the single-channel system. This slightly increases the VA rating of the primary-side circuits.

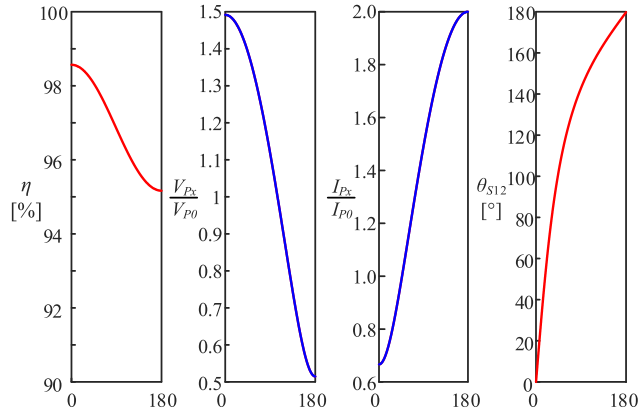

Fig. 11. Efficiency, input voltage, primary currents, and phase difference between two primary currents as functions of the phase difference of two secondary currents for the system with $k_{P1S1} = k_{P2S1} = 0.1$ (other cross couplings are zero).

As for the system with $k_{S1S2} = -0.1$, the system efficiency drops by 0.2%, as shown in Fig. 10, which agrees with the previous analysis. Moreover, the secondary-side cross coupling causes unbalance in both the primary currents and the input voltages when the phase difference of two secondary currents is not 0° or 180°.

With nonzero intersides cross couplings, the efficiency could be higher or lower than the efficiency of the single-channel counterpart, as shown in Fig. 11. In the case with $k_{P1S1} = k_{P2S1} = 0.1$, the efficiency is improved by about 0.5% when the secondary currents are in-phase. This means each of the primary currents will deliver active power to both the secondary windings, which is a more energy-efficient way than the original single-channel system. However, when the secondary currents are totally out of phase as desired to eliminate the stray B-field, a significant efficiency drop appears. If the coupling coefficients become negative as when the lateral distance of two windings is large enough, this conclusion changes to the opposite, i.e., 0° phase angle of the secondary currents leads to efficiency drop and 180° out of phase increases the efficiency.

IV. THREE-CHANNEL WPT SYSTEM

A. Prototype Magnetic Coupler Design

Similar to the analysis of Section III, interside cross couplings in the three-channel WPT system presented below will also lead to a serious efficiency drop when the secondary-side resonators transmit real power to the primary-side resonators. Likewise, primary-side cross couplings will increase the required input voltage of the system to generate the required output currents and cause input voltage unbalance when the phase difference of the output currents is not 0° or 180°, whereas the secondary-side cross couplings will slightly decrease the system efficiency and increase the primary currents, also cause input voltage and primary current unbalance when the phase difference of the output currents is not 0° or 180°. Moreover, all of the cross couplings form additional power paths in the system for either real power or reactive power or both. These power paths become serious challenges when trying to control the current amplitudes and

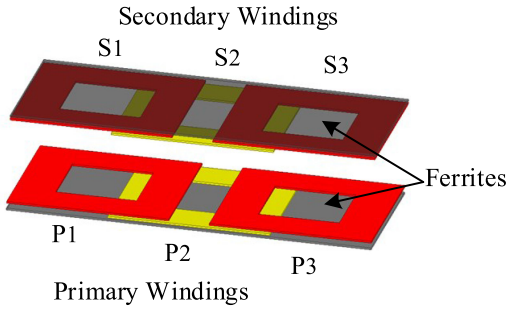

Fig. 12. Three-channel WPT system with decoupled neighboring windings.

TABLE III
COUPLING COEFFICIENTS OF THE PADS IN FIG. 12

k_{P1S1}, k_{P2S2}, k_{P3S3}	k_{P1S2}, k_{S2P3}	k_{S1P2}, k_{P2S3}	k_{P1S3}, k_{S1P3}
0.195, 0.198, 0.195	**0.033**	**0.029**	**-0.060**
k_{S1S2}, k_{S2S3}	k_{S1S3}	k_{P1P3}	k_{P1P2}, k_{P2P3}
-0.004	-0.079	-0.086	-0.005

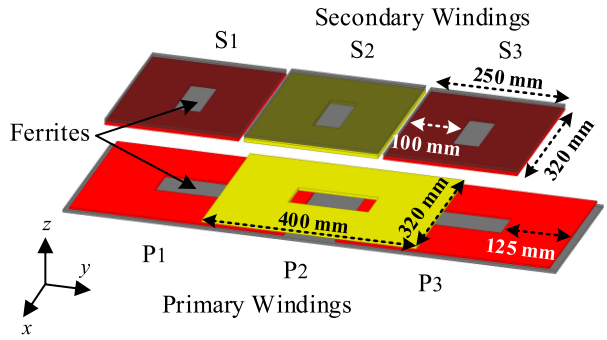

Fig. 13. Asymmetric pad design for the three-channel WPT system.

TABLE IV
COUPLING COEFFICIENTS OF THE PROTOTYPE

k_{P1S1}, k_{P3S3}	k_{P2S2}	k_{P1S2}, k_{S2P3}	k_{S1P2}, k_{P2S3}	k_{P1S3}, k_{S1P3}
0.157	0.176	**0.006**	**-0.0007**	**-0.024**
k_{S1S2}, k_{S2S3}	k_{S1S3}	k_{P1P3}	k_{P1P2}, k_{P2P3}	
-0.053	-0.012	-0.055	0.004	

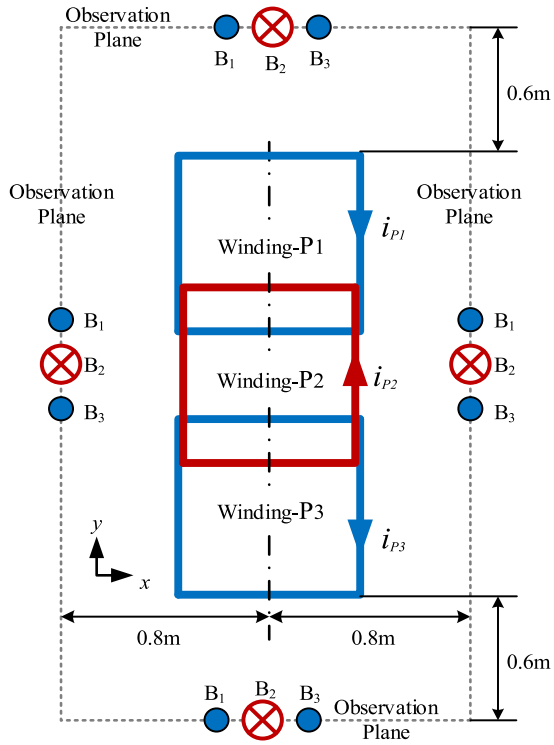

Fig. 14. Top view of the magnetic field directions and cancelation mechanism of the primary windings.

phase angles, as desired to eliminate the stray B-field. Therefore, in designing a multichannel WPT system, all cross couplings should be minimized, especially from the control point of view. However, it is usually impossible to eliminate all the cross couplings by designing the structure of the couplers. Moreover, there are also other considerations in practical implementations, such as compact receiving pads.

Straightforward, the method of adding an overlap to decouple two neighboring windings [14], [25] can be adopted to deal with the same-side cross couplings. This three-winding structure is exactly the same as a DDQ pad developed in [25], [46], and [47], which can significantly enhance the misalignment performance of a WPT system. But it should be noted that a DDQ pad does not require perfect decoupling between two neighboring windings as the three-winding structure in Fig. 12 does. By repeating this structure, every two adjacent windings in either the primary or the secondary side can be decoupled, as shown in Fig. 12, but the interside cross couplings will still be present. In the simulations, plate ferrite structure is adopted for better performance [41]. The simulation results of the coupling coefficients are given in Table III.

An asymmetric structure is proposed to eliminate those diagonal couplings and produce more compact receiving windings, as shown in Fig. 13. The windings of the primary (or secondary) side are using a partially overlapping structure, whereas the windings of the other side use smaller windings. The air gap of the prototype is determined to be 160 mm for a fair comparison with the results obtained in [9]. The coupling coefficients of the windings are given in Table IV. Compared with that in Table III, the diagonal couplings' coefficients, as shown in bold, have been significantly reduced.

After properly eliminating the undesired cross couplings, currents with 180° phase difference can be injected into two neighboring windings, as suggested by Fig. 14, and thus, they generate canceling magnetic fields outside the winding area. Taking the primary windings as an example, Fig. 14 visualizes the field cancelation mechanism from a top view. The currents in windings $P1$ and $P3$ are in the same direction, while that of winding-$P2$ is in the opposite direction. As a result, the magnetic field generated by winding-$P2$ is always canceling that generated by windings $P1$ and $P3$ outside the winding area. In the three-winding array, as shown in Fig. 13, windings $P1$ and $P3$ are designed to be identical and have the same current direction and amplitude. Therefore, it is reasonable to have a larger MMF (i.e., NI) in the middle winding so that the field cancelation will

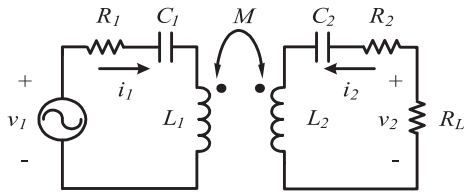

Fig. 15. Lumped circuit model of a single-channel WPT system.

be more comprehensive, as also indicated in Fig. 14. Case studies are carried out to determine the optimal power-sharing ratio among the channels for minimizing stray magnetic flux density on the observation planes. Based on the dimensions given in Fig. 13, the windings are designed separately for each channel. The wire is supposed to conduct 4 A/mm^2 of the sectional area. The dc input voltage fed to the primary-side inverter of each channel is 800 V, and the dc output voltage is 600 V. The rated power is 50 kW, and the operating frequency is 85 kHz. The number of strands (diameter of strand 0.1 mm) of the wire for each winding can then be determined with a given power-sharing ratio among the channels. The number of turns of the windings is determined with the same method of designing a single-channel WPT system, which is described as follows.

Fig. 15 shows the lumped circuit model of a single-channel WPT system. The KVL equations of this model are given by

$$\begin{bmatrix} \mathbf{V_1} \\ \mathbf{0} \end{bmatrix} = \begin{bmatrix} R_1 + j\left(\omega L_1 - \frac{1}{\omega C_1}\right) & j\omega M \\ j\omega M & R_2 + R_L + j\left(\omega L_2 - \frac{1}{\omega C_2}\right) \end{bmatrix} \cdot \begin{bmatrix} \mathbf{I_1} \\ \mathbf{I_2} \end{bmatrix}. \tag{16}$$

If both the transmitter and the receiver resonate at the operating frequency, the rms values of the secondary current I_2 and primary current I_1 can be derived as

$$I_2 = \sqrt{\frac{P_o}{R_L}} \tag{17}$$

$$I_1 = \frac{R_L + R_2}{2\pi f M} I_2. \tag{18}$$

If the parasitic resistance is neglected, the output voltage of the system equals the induced voltage in the secondary side

$$V_2 = \omega M I_1 \tag{19}$$

where V_2 is the rms value of the load voltage v_2. On the other hand, if the input voltage of the system, i.e., V_1, is given, the winding current I_1 is determined by the rated power of the system. Thus, the required mutual inductance of the system at the rated operation point is given by (19). The number of turns of the windings can then be determined to create the required mutual inductance. Multiple solutions for the numbers of turns of the transmitting and receiving windings might exist for given winding and wire dimensions. An empirical practice is to balance the numbers of turns of both windings, considering the sizes and the thermal management ability of the windings.

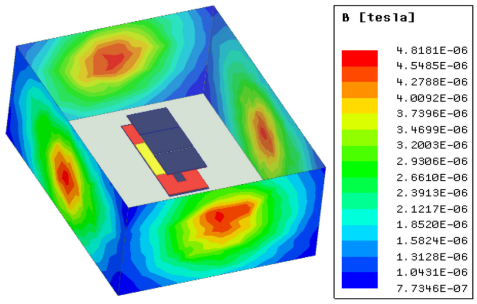

Fig. 16. FEA simulation result of the magnetic flux density on the observation planes (total pads area = 0.53 m^2).

B. FEA Simulation Outcomes

After the parameters of the windings are determined, the amplitude values of the currents (already calculated from the given input voltage, output voltage, rated power, and power-sharing ratio) are used as excitation in finite-element analysis (FEA) simulations. The current directions of each of the two neighboring windings are opposite. The simulation results are given in Table V. It is evident from the results that the field cancelation mechanism has been utilized to significantly reduce the magnetic field at the observation distance. The optimized power-sharing ratio should be that the middle channel outputs larger power than the aside channels. In this case study, the optimal power distribution is close to 2:6:2, achieving an 80% reduction in the stray magnetic field compared with the measured value of the single-channel system, as reported in [9] (i.e., 24 μT). While compared with the measured value of the system using DD pads, which is also given in [9] (i.e., 13 μT), the reduction is 63%. By using average power distribution, the reductions are 58% and 23% with respect to 24 and 13 μT, respectively. However, other factors, such as cooling system design, should be considered in real applications, and therefore, it might be easier for practical design and implementation by using identical pads for all the channels. In this article, the power ratio of 3:4:3 is adopted to demonstrate the significance of the power ratio on the stray magnetic field attenuation. The FEA simulation setup and the result of the optimal case are shown in Fig. 16.

Another comparison is provided between the three-channel system and another single-channel system with compact pads. Details of the single-channel system with aluminum shielding plates are provided in Table VI. The system is designed to output 50 kW at the same input and output voltages, i.e., 800 V and 600 V, respectively, and the same air gap of 160 mm. The windings and ferrite layers are identical, but the shielding layer on the secondary side is larger, as suggested by the SAE [13]. The maximum stray B-field at 0.8 m distance is 10.2 μT, as shown in Fig. 17(a). If the shielding layers are removed, the stray B-field becomes 26.9 μT, as shown in Fig. 17(b). The B-field attenuation of the shielding layers is consistent with the results reported in [24].

TABLE V
EFFECT OF POWER-SHARING RATIO OF CHANNELS

Power Sharing Ratio	1.5:7:1.5 (middle channel outputs 70% of the total power)	2:6:2 (middle channel outputs 60% of the total power)	3:4:3 (middle channel outputs 40% of the total power)	1:1:1 (average distribution)
Wire of Winding-P1 and -P3	0.1 mm × 350 strands outer diameter 2.62 mm	0.1 mm × 450 strands outer diameter 3.00 mm	0.1 mm × 700 strands outer diameter 3.70 mm	0.1 mm × 750 strands outer diameter 3.83 mm
Number of turns of Winding-P1 and-P3	46	41	33	32
Wire of Winding-S1 and -S3	0.1 mm × 450 strands outer diameter 3.00 mm	0.1 mm × 600 strands outer diameter 3.43 mm	0.1 mm × 900 strands outer diameter 4.20 mm	0.1 mm × 1000 strands outer diameter 4.43 mm
Number of turns of Winding-S1 and -S3	33	28	23	22
Wire of Winding-P2	0.1 mm × 1600 strands outer diameter 5.60 mm	0.1 mm × 1350 strands outer diameter 5.15 mm	0.1 mm × 900 strands outer diameter 4.20 mm	0.1 mm × 750 strands outer diameter 3.83 mm
Number of turns of Winding-P2	21	23	29	30
Wire of Winding-S2	0.1 mm × 2100 strands outer diameter 6.42 mm	0.1 mm × 1800 strands outer diameter 5.94 mm	0.1 mm × 1200 strands outer diameter 4.85 mm	0.1 mm × 1000 strands outer diameter 4.43 mm
Number of turns of Winding-S2	15	16	19	22
Maximum B-field (RMS) at the observation plans at 50 kW	5.5 μT	4.8 μT	8.2 μT	10 μT
Reduction compared with the single-channel in [9] (i.e., 24 μT)	77%	80%	66%	58%
Reduction compared with the system with DD pads in [9] (i.e., 13 μT)	58%	63%	37%	23%

TABLE VI
DIMENSION OF THE TWO IDENTICAL PADS IN Fig. 17

Winding dimension (mm)	Outer: 400×400 Inner: 160×160 Single layer	Primary winding wire	Ø7.25mm (Ø0.1mm×2500)
Ferrite dimension (mm)	420×420×5	Secondary winding wire	Ø7.94mm (Ø0.1mm×3000)
Aluminum Shield dimension (mm)	Pri.: 450×450×3 Sec.: 600×600×3	Number of turns	Pri. 13 Sec. 10
Gap between winding and ferrite (mm)	2	Gap between ferrite and shield (mm)	10
Inductances		Pri. 94.7μH, Sec. 55.6μH, *M* 14.3μH	

For the three-channel system, the effect of shielding layers (pri.: 350 mm × 950 mm × 3 mm; sec.: 500 mm × 900 mm × 3 mm; and the gap between ferrite and shield: 10 mm) is investigated in Fig. 18. After adding the shields, the stray B-field becomes a bit higher than that in Fig. 16. This is consistent with the observation that shielding layers might increase the stray B-field of BPPs, as reported in [15]. Nevertheless, the stray B-field of the shielded three-channel system is still 45% lower than that of the shielded single-channel system with compact pads.

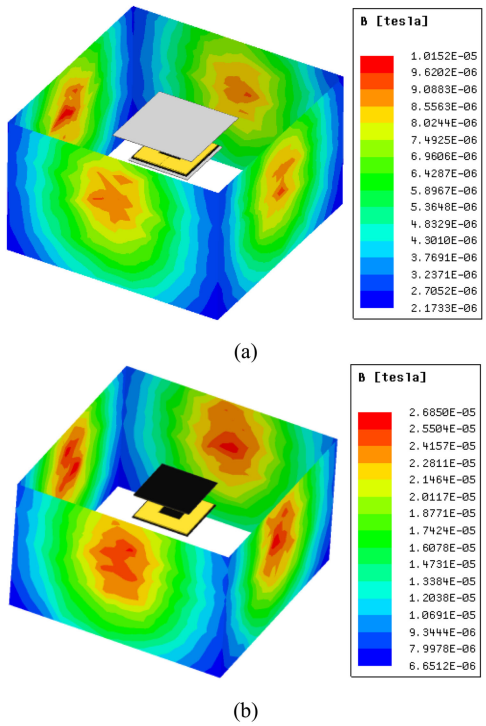

Fig. 17. Simulation results of the single-channel system with compact pads. (a) With an aluminum shielding layer. (b) Without shielding.

V. EXPERIMENTAL VERIFICATION

A. Setup for Experiments

The inductances of the system with a 3:4:3 power ratio, as described in Table V, are obtained from FEA simulation and then used in a circuit simulator to estimate the performance of the system. Using the design of power ratio 3:4:3 in Table V, the output power is lower than 50 kW according to circuit simulations when all cross couplings are included. Therefore, the number of turns of winding-*P*2 is reduced to 25 so that the mutual inductance is smaller and can transmit more power for a given input voltage. The wire of windings *P*2 and *S*2 is changed to 1000 and 1300 strands, respectively, for higher current carrying ability. The other parameters are unchanged.

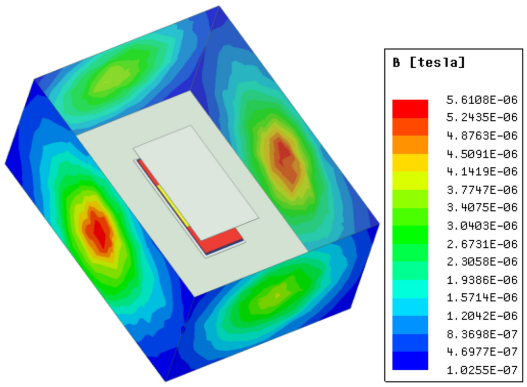

Fig. 18. Simulation results of the three-channel system with shielding layers.

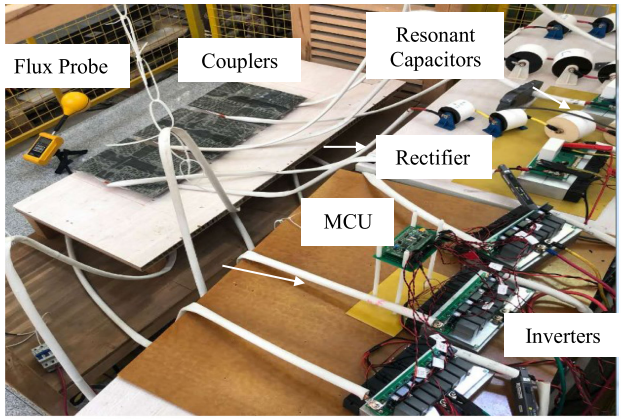

(a)

(b)

Fig. 19. Experimental setup. (a) Aerial view. (b) Flux density observation point.

The photographs of the complete setup are displayed in Fig. 19, and Table VII presents the measured inductances compared with the simulation results. Note that the little disagreement between the measured and simulated values of the inductances in Table V was largely due to lengthy terminals of the prototype windings and other factors, such as imperfect edges of the rectangles in the constructed windings. The compensating capacitances of the prototype are listed in Table VIII.

The topology in Fig. 2 is adopted for the prototype. A three-phase transformer and a three-phase rectifier channel are used to generate the desired input dc voltage. The inverters are developed using MOSFET C2M0025120D from Cree. Two

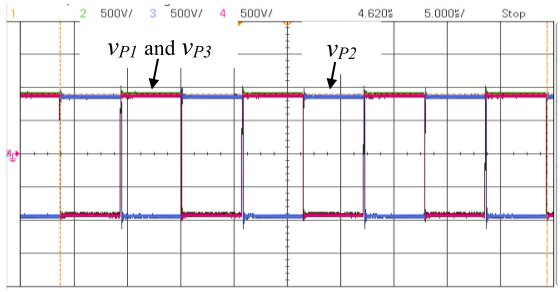

(a)

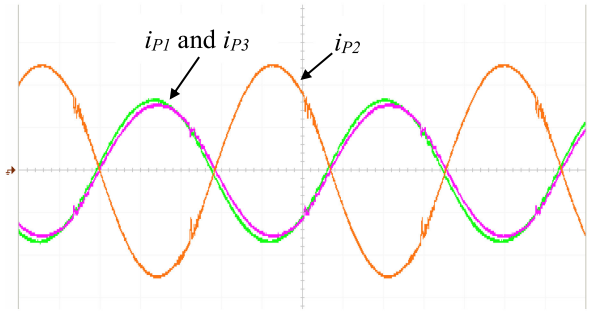

(b)

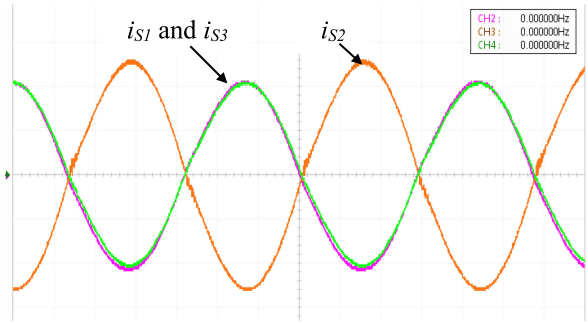

(c)

Fig. 20. Waveforms at rated power of 50 kW. (a) Inverter output voltage: 500 V/div and time: 5 μs/div. (b) Primary windings current: 20 A/div and time: 2 μs/div. (c) Secondary windings current: 20 A/div and time: 2 μs/div.

discrete MOSFETs with a common gate driving signal are used in parallel for each switch of the full-bridge inverter, to guarantee the current carrying capacity of up to 20 kW of each inverter. Eight number of 5 μF, 900 V dc-link capacitor is used on each inverter with a layout similar to what is obtained in [42]. For the full-bridge rectifier, a diode RURG80100 from Infineon is adopted, having a single device on each switch. A film capacitor of 20 μF, 1.1 kV is placed at the output of each rectifier. The approach to thermal management of the identical converters is similar to that of the article presented in [43]. The load resistance is fixed at 7.2 Ω for different output powers. Magnetic flux density is measured using Narda ELT-400 flux probe and Yokogawa WT1800 precision power analyzer is used to capture the dc–dc efficiency.

B. Results and Discussion

Waveforms of the primary and secondary winding currents at 50 kW rated power are captured and given in Fig. 20. The

TABLE VII
INDUCTANCES OF WINDINGS

	L_{P1}	L_{S1}	L_{P2}	L_{S2}	L_{P3}	L_{S3}	M_{P1S1}	M_{P1P2}	M_{P1S2}	M_{P1P3}	M_{P1S3}
Simulation	509.9	181.8	265.1	123.5	507.9	182.0	47.90	1.38	1.53	-28.06	-7.17
Measured	505.7	180.3	259.8	124	506.9	186	51	0.25	2.75	-23.00	-5.60
	M_{S1P2}	M_{S1S2}	M_{S1P3}	M_{S1S3}	M_{P2S2}	M_{P2P3}	M_{P2S3}	M_{S2P3}	M_{S2S3}	M_{P3S3}	
Simulation	-0.135	-7.91	-7.14	-2.17	31.80	1.36	-0.130	1.53	-7.93	47.85	
Measured	-0.45	-5.85	-5.13	-1.75	34.5	0.25	-1.25	-1	-6.25	49.03	

TABLE VIII
COMPENSATING CAPACITANCES OF THE PROTOTYPE

C_{P1}	C_{S1}	C_{P2}	C_{S2}	C_{P3}	C_{S3}
7.1 nF	20.5 nF	12.6 nF	28.1 nF	7.5 nF	20.4 nF

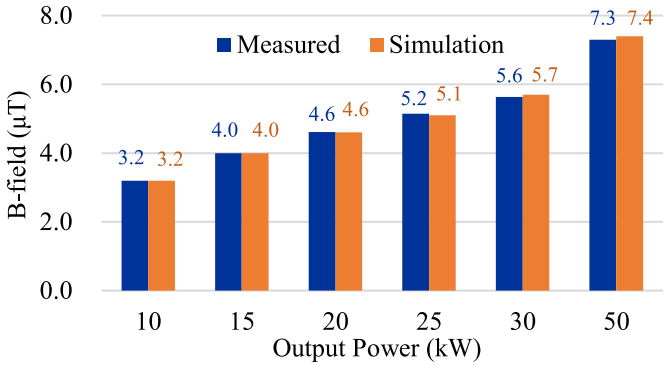

Fig. 21. Measured magnetic flux density at the observation point compared with the simulation result.

currents of the middle channel, i.e., i_{P2} and i_{S2}, are basically 180° out of phase with the currents of the aside channels, i.e., i_{P1} and i_{P3}, and i_{S1} and i_{S3}. In both the primary and secondary sides, the middle windings have larger currents than the two adjacent windings and the middle receiving winding outputs 39.3% of the total power, which is close to the designed value.

The magnetic flux density is measured at an 80 cm distance from the midpoint of the couplers under perfectly aligned condition, as displayed in Fig. 19(b). It should be noted that this point does not necessarily have the maximum B-field. However, it is difficult to precisely locate a point in three-dimensional space in practice. Therefore, the measured B-field at this said point is first compared with the FEA simulation results at the same point, as given in Fig. 21, when the output power is increased from 10 to 50 kW. In the FEA simulations, the windings' currents are obtained in circuit simulations with the circuit topology, as given in Fig. 2, and with the measured inductances and capacitances. It is obvious from Fig. 21 that the simulation results are basically identical with the measured ones. Then, we can easily obtain the maximum stray B-field on the observation plane in the simulation. As shown in Fig. 22, the maximum stray B-field is 8.0 μT when the phase angle of the primary current i_{P1} is about 30°. Compared with the benchmark value of 24 μT

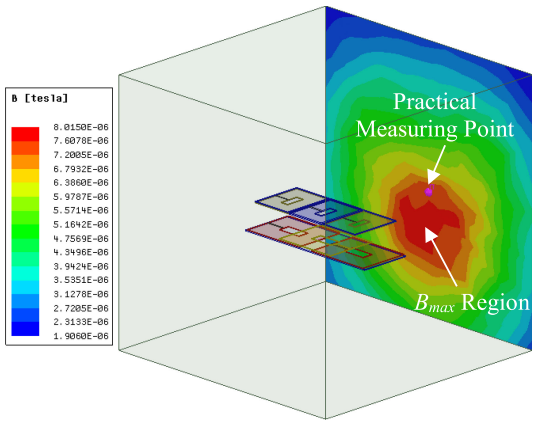

Fig. 22. Simulation of maximum B-field on the observation plane at 50 kW.

(a)

(b)

Fig. 23. Measured dc–dc efficiencies. (a) Output power of 50 kW. (b) Output power of 5 kW with only the inverter of the aside channel ($P1$–$S1$) activated.

(single-channel system) and 13 μT (DD pads) [9], the reduction is, respectively, 66.7% and 38.5%.

The efficiency performance of the system has been carefully investigated. Since the proposed system consists of three traditional WPT systems, which are basically decoupled with

each other, the efficiency of the proposed system was expected to be close to that of the traditional single-channel system. The screen capture of the power analyzer indicating the dc–dc efficiency at 50 kW is 95.2%, as shown in Fig. 23(a). When the output power is lower than the rated power of one of the channels, only one channel is activated to push up the light-load efficiency. It should be noted that the other two channels are not disconnected from the system under this operation. Therefore, the nonactivated channels also experience some power flows, which might degrade the efficiency. Even so, the efficiency at one-tenth of the full power, i.e., 5 kW, is still as high as 93.3%, which is only 1.8% lower than the full-load efficiency, as given in Fig. 23(b).

VI. Conclusion

The concept of multichannel WPT exposes a new approach to develop the high-power WPT systems under stringent safety requirement and efficiency performance. The design of a three-channel WPT system with minimized cross couplings is presented so that the amplitudes and phase angles of the winding current in each channel can be easily regulated without the interference of other channels. A three-channel WPT of 50 kW is conceptualized and simulated. The simulation results are compared against the conventional single-channel WPT systems of the same power rating, and the reduction in the stray B-field turns out to be 78% (compared with circular pad) and 63% (compared with DD pad) when the power-sharing ratio is 2:6:2. A prototype with a power-sharing ratio of 3:4:3 is built and the performance of the system at the maximum rated power of 50 kW is measured. The measured stray B-field verifies the simulation results. The efficiency performance of the prototype is considerably appreciable.

This design is perfect for self-driving vehicles with high positioning accuracy. In both research and commercially available products, the positioning accuracy of self-driving vehicles, such as automated guided vehicles, has been reported to be within several millimeters [44], [45]. Considering the fast-developing speed of self-driving techniques, self-driving vehicles with high positioning accuracy will surely be popularized in the near future, and thus, misalignment will be no longer an issue. On the other hand, the field cancelation and cross-coupling minimizing design procedure could be harnessed to provide an alternative technique for developing a high-power WPT system with low stray magnetic fields and reasonable efficiency performance. This is promising in developing fast wireless charging systems and promotes the competition of EVs.

References

[1] N. Tesla, "High frequency oscillators for electro-therapeutic and other purposes," in *The Electrical Engineer*, vol. 26. Buffalo, MN, USA, Biggs & Company, Nov. 1898, no. 550.

[2] S. Y. R. Hui, "Magnetic resonance for wireless power transfer [A look back]," *IEEE Power Electron. Mag.*, vol. 3, no. 1, pp. 14–31, Mar. 2016.

[3] G. A. Covic and J. T. Boys, "Inductive power transfer," *Proc. IEEE*, vol. 101, no. 6, pp. 1276–1289, Jun. 2013.

[4] S. Li and C. C. Mi, "Wireless power transfer for electric vehicle applications," *IEEE J. Emerg. Sel. Topics Power Electron.*, vol. 3, no. 1, pp. 4–17, Mar. 2015.

[5] R. Bosshard and J. W. Kolar, "Multi-objective optimization of 50 kW/85 kHz IPT system for public transport," *IEEE J. Emerg. Sel. Topics Power Electron.*, vol. 4, no. 4, pp. 1370–1382, Dec. 2016.

[6] J. Shin *et al.*, "Design and implementation of shaped magnetic-resonance-based wireless power transfer system for roadway-powered moving electric vehicles," *IEEE Trans. Ind. Electron.*, vol. 61, no. 3, pp. 1179–1192, Mar. 2014.

[7] S. Y. Choi, B. W. Gu, S. Y. Jeong, and C. T. Rim, "Advances in wireless power transfer systems for roadway-powered electric vehicles," *IEEE J. Emerg. Sel. Topics Power Electron.*, vol. 3, no. 1, pp. 18–36, Mar. 2015.

[8] J. H. Kim *et al.*, "Development of 1-MW inductive power transfer system for a high-speed train," *IEEE Trans. Ind. Electron.*, vol. 62, no. 10, pp. 6242–6250, Oct. 2015.

[9] R. Bosshard, U. Iruretagoyena, and J. W. Kolar, "Comprehensive evaluation of rectangular and double-D coil geometry for 50 kW/85 kHz IPT system," *IEEE J. Emerg. Sel. Topics Power Electron.*, vol. 4, no. 4, pp. 1406–1415, Dec. 2016.

[10] J. Pries, V. P. N. Galigekere, O. C. Onar, and G.-J. Su, "A 50-kW three-phase wireless power transfer system using bipolar windings and series resonant networks for rotating magnetic fields," *IEEE Trans. Power Electron.*, vol. 35, no. 5, pp. 4500–4517, May 2020.

[11] V. P. Galigekere *et al.*, "Design and Implementation of an optimized 100 kW stationary wireless charging system for EV battery recharging," in *Proc. IEEE Energy Convers. Congr. Expo.*, Portland, OR, USA, 2018, pp. 3587–3592.

[12] ICNIRP Guidelines, "Guidelines for limiting exposure to time-varying electric and magnetic fields (1 Hz to 100 kHz)," *Health Phys.*, vol. 99, no. 6, pp. 818–836, 2010.

[13] "Wireless power transfer for light-duty plug-in/electric vehicles and alignment methodology," *SAE Int.*, Warrendale, PA, USA, pp. 29–32, May 2016.

[14] S. Kim, G. A. Covic, and J. T. Boys, "Tripolar pad for inductive power transfer systems for EV charging," *IEEE Trans. Power Electron.*, vol. 32, no. 7, pp. 5045–5057, Jul. 2017.

[15] M. Mohammad *et al.*, "Design of an EMF suppressing magnetic shield for a 100-kW DD-coil wireless charging system for electric vehicles," in *Proc. IEEE Appl. Power Electron. Conf. Expo.*, Anaheim, CA, USA, 2019, pp. 1521–1527.

[16] S. Y. R. Hui and S. C. Tang, "Planar printed circuit-board transformers with effective electromagnetic interference (EMI) shielding," U.S. Patent 09/883 145, 2003.

[17] M. Budhia, G. A. Covic, and J. T. Boys, "Design and optimization of circular magnetic structures for lumped inductive power transfer systems," *IEEE Trans. Power Electron.*, vol. 26, no. 11, pp. 3096–3108, Nov. 2011.

[18] Y. Yashima, H. Omori, T. Morizane, N. Kimura, and M. Nakaoka, "Leakage magnetic field reduction from wireless power transfer system embedding new eddy current-based shielding method," in *Proc. Int. Conf. Elect. Drives Power Electron.*, Tatranska Lomnica, Slovakia, 2015, pp. 241–245.

[19] J. Kim *et al.*, "Coil design and shielding methods for a magnetic resonant wireless power transfer system," *Proc. IEEE*, vol. 101, no. 6, pp. 1332–1342, Jun. 2013.

[20] M. Lu and K. D. T. Ngo, "Comparison of passive shields for coils in inductive power transfer," in *Proc. IEEE Appl. Power Electron. Conf. Expo.*, Tampa, FL, USA, 2017, pp. 1419–1424.

[21] Q. Zhu, Y. Zhang, Y. Guo, C. Liao, L. Wang, and Lifang Wang, "Null-coupled electromagnetic field canceling coil for wireless power transfer system," *IEEE Trans. Transp. Electrific.*, vol. 3, no. 2, pp. 464–473, Jun. 2017.

[22] M. Lu and K. D. T. Ngo, "Circuit models and fast optimization of litz shield for inductive-power-transfer coils," *IEEE Trans. Power Electron.*, vol. 34, no. 5, pp. 4678–4688, May 2019.

[23] S. Y. Choi, B. W. Gu, S. W. Lee, W. Y. Lee, J. Huh, and C. T. Rim, "Generalized active EMF cancel methods for wireless electric vehicles," *IEEE Trans. Power Electron.*, vol. 29, no. 11, pp. 5770–5783, Nov. 2014.

[24] H. Cui, W. Zhong, H. Li, F. He, M. Chen, and D. Xu, "A study on the shielding for wireless charging systems of electric vehicles," in *Proc. IEEE Appl. Power Electron. Conf. Expo.*, 2018, pp. 1336–1343.

[25] M. Budhia, G. A. Covic, J. T. Boys, and C.-Y. Huang, "Development and evaluation of single sided flux couplers for contactless electric vehicle charging," in *Proc. IEEE Energy Convers. Congr. Expo.*, Sep. 2011, pp. 614–621.

[26] J. Gao, "Traveling magnetic field for homogeneous wireless power transmission," *IEEE Trans. Power Del.*, vol. 22, no. 1, pp. 507–514, Jan. 2007.

[27] G. A. Covic, J. T. Boys, M. L. G. Kissin, and H. G. Lu, "A three-phase inductive power transfer system for roadway-powered vehicles," *IEEE Trans. Ind. Electron.*, vol. 54, no. 6, pp. 3370–3378, Dec. 2007.

[28] H. Matsumoto, Y. Neba, K. Ishizaka, and R. Itoh, "Model for a three-phase contactless power transfer system," *IEEE Trans. Power Electron.*, vol. 26, no. 9, pp. 2676–2687, Sep. 2011.
[29] D. J. Thrimawithana and U. K. Madawala, "A three-phase bi-directional IPT system for contactless charging of electric vehicles," in *Proc. IEEE Int. Symp. Ind. Electron.*, Jun. 2011, pp. 1957–1962.
[30] W. M. Ng, C. Zhang, D. Lin, and S. Y. R. Hui, "Two- and three-dimensional omnidirectional wireless power transfer," *IEEE Trans. Power Electron.*, vol. 29, no. 9, pp. 4470–4474, Sep. 2014.
[31] H. Matsumoto, Y. Neba, H. Iura, D. Tsutsumi, K. Ishizaka, and R. Itoh, "Trifoliate three-phase contactless power transformer in case of winding-alignment," *IEEE Trans. Ind. Electron.*, vol. 61, no. 1, pp. 53–62, Jan. 2014.
[32] A. Abdolkhani, A. P. Hu, and J. Tian, "Autonomous polyphase current-fed push–pull resonant converter based on ring coupled oscillators," *IEEE J. Emerg. Sel. Topics Power Electron.*, vol. 3, no. 2, pp. 568–576, Jun. 2015.
[33] M. L. G. Kissin, J. T. Boys, and G. A. Covic, "Interphase mutual inductance in polyphase inductive power transfer systems," *IEEE Trans. Ind. Electron.*, vol. 56, no. 7, pp. 2393–2400, Jul. 2009.
[34] Y. Song, U. K. Madawala, T. Duleepa J, and A. P. Hu, "Cross-coupling effects of poly-phase bi-directional inductive power transfer systems used for EV charging," in *Proc. IEEE 2nd Int. Future Energy Electron. Conf.*, Nov. 2015, pp. 1–7.
[35] K. Kusaka, K. Furukawa, and J.-I. Itoh, "Radiative noise reduction technique using 12 coils suitable for high-power inductive power transfer," in *Proc. IEEE Energy Convers. Congr. Expo.*, Portland, OR, USA, 2018, pp. 6179–6186.
[36] T. Shijo, K. Ogawa, M. Suzuki, Y. Kanekiyo, M. Ishida, and S. Obayashi, "EMI reduction technology in 85 kHz band 44 kW wireless power transfer system for rapid contactless charging of electric bus," in *Proc. IEEE Energy Convers. Congr. Expo.*, Milwaukee, WI, USA, 2016, pp. 1–6.
[37] A. Safaee, K. Woronowicz, and T. Dickson, "Reactive power compensation in three phase high output inductive power transfer," in *Proc. IEEE Elect. Power Energy Conf* ., Oct. 2015, pp. 375–380.
[38] M. Misakian "Equations for the magnetic field produced by one or more rectangular loops of wire in the same plane" *J. Res. Nat. Inst. Standards Technol.*, vol. 105, no. 4, pp. 557–564, Jul./Aug. 2000.
[39] A. Mocholí-Salcedo, J. H. Arroyo-Núñez, V. M. Milián-Sánchez, M. J. Palomo-Anaya, and A. Arroyo-Núñez, "Magnetic field generated by the loops used in traffic control systems," *IEEE Trans. Intell. Transp. Syst.*, vol. 18, no. 8, pp. 2126–2136, Aug. 2017.
[40] E. Weber, *Electromagnetic Fields: Theory and Applications*, vol. 1. Hoboken, NJ, USA: Wiley, 1952, pp. 129–1134.
[41] W. Zhong, H. Cui, H. Li, A. U. Ibrahim, and D. Xu, "Study on the effect of ferrite layers in a wireless charging system with automotive chassis," in *Proc. IEEE Int. Power Electron. Appl. Conf. Expo.*, Shenzhen, China, 2018, pp. 1–6.
[42] R. Bosshard and J. W. Kolar, "All-SiC 9.5 kW/dm^3 on-board power electronics for 50 kW/85 kHz automotive IPT system," *IEEE J. Emerg. Sel. Topics Power Electron.*, vol. 5, no. 1, pp. 419–431, Mar. 2017.
[43] N. He, M. Chen, J. Wu, N. Zhu, and D. Xu, "20-kW zero-voltage-switching SiC-mosfet grid inverter with 300 kHz switching frequency," *IEEE Trans. Power Electron.*, vol. 34, no. 6, pp. 5175–5190, Jun. 2019.
[44] Y. Zhuang *et al.*, "A survey of positioning systems using visible LED lights," *IEEE Commun. Surv. Tut.*, vol. 20, no. 3, pp. 1963–1988, Jul./Sep. 2018.
[45] "The most accurate laser positioning system for autonomous mobile robots." [Online]. Available: https://www.guidanceautomation.com/agv-navigation-systems/beacon/, Accessed on: Apr. 4, 2020.
[46] M. Budhia, J. T. Boys, G. A. Covic, and C.-Y. Huang, "Development of a single-sided flux magnetic coupler for electric vehicle IPT charging systems," *IEEE Trans. Ind. Electron.*, vol. 60, no. 1, pp. 318–328, Jan. 2013.
[47] A. Ahmad, M. S. Alam, and A. A. S. Mohamed, "Design and interoperability analysis of quadruple pad structure for electric vehicle wireless charging application," *IEEE Trans. Transp. Electrific.*, vol. 5, no. 4, pp. 934–945, Dec. 2019.
[48] R. Syms, E. Shamonina, and L. Solymar, "Magneto-inductive waveguide devices," *Proc. Inst. Elect. Eng.–Microw., Antennas Propag.*, vol. 153, no. 2, pp. 111–121, Apr. 2006.
[49] C. K. Lee, W. X. Zhong , and S. Y. R. Hui, "Effects of magnetic coupling of nonadjacent resonators on wireless power domino-resonator systems," in *IEEE Transa. Power Elect.*, vol. 27, no. 4, pp. 1905–1916, Apr. 2012, doi: 10.1109/TPEL.2011.2169460.

Abubakar Uba Ibrahim (Student Member, IEEE) received the B.Eng. degree in electrical engineering from Bayero University Kano, Kano, Nigeria, in 2008, and the M.Sc. degree in electronics and electrical engineering from Strathclyde University, Glasgow, U.K., in 2012. He is currently working toward the Ph.D. degree with the Department of Electrical and Electronic Engineering, Zhejiang University, Hangzhou, China.

His research interests include wireless power transfer technologies and their driving power converters.

Wenxing Zhong (Member, IEEE) received the B.Eng. degree in electrical engineering from Tsinghua University, Beijing, China, in 2007, and the Ph.D. degree from the City University of Hong Kong, Hong Kong, in 2012.

He is currently a Professor with the Department of Electrical Engineering, Zhejiang University, Hangzhou, China. From March 2016 to May 2017, he was a Research Assistant Professor with the Department of Electrical and Electronics Engineering, University of Hong Kong, Hong Kong. His research interests include wireless power transfer and power electronics.

Dr. Zhong was a recipient of two Transactions First Prize Paper Awards from IEEE Power Electronics Society.

Mark Dehong Xu (Fellow, IEEE) received the Ph.D. degree from the Department of Electrical Engineering, Zhejiang University, Hangzhou, China, in 1989.

Since 1996, he has been a Full Professor with Zhejiang University. He was a Visiting Professor with the Department of Electrical Engineering, University of Tokyo, Japan, from May 1995 to June 1996, with the Center of Power Electronics System, Virginia Tech, USA, from June 2000 to December 2000, and with the Power Electronics Lab, ETH, Zurich, from February 2006 to April 2006. He has authored 10 books and more than 200 IEEE Journal or Conference papers. He holds more than 40 patents. His research interests include power electronics topology, control, and applications to renewable energy and energy efficiency.

Dr. Xu was a recipient of six IEEE Transaction or Conference Prize Paper Awards, and the IEEE PELS R. D. Middlebrook Achievement Award, in 2016. He was an IEEE PELS Distinguish Lecturer from 2015 to 2018. He was an At-large Adcom Member of IEEE Power Electronics Society from 2020 to 2022. He is the Co-Editor-Chief of the *IEEE Open Journal of Power Electronics* and an Associate Editor for the IEEE TRANSACTIONS ON POWER ELECTRONICS. He was the General Chair of the IEEE International Symposium on Industrial Electronics (ISIE2012, Hangzhou), IEEE International Symposium on Power Electronics for Distributed Generation Systems (PEDG2013, Arkansas), and IEEE International Power Electronics and Applications Conference (PEAC2018, Shenzhen).